Wood Sci Technol (2012) 46:769–779
DOI 10.1007/s00226-011-0442-y

ORIGINAL

Automated quantification of the impact of the wood-decay fungus *Physisporinus vitreus* on the cell wall structure of Norway spruce by tomographic microscopy

M. J. Fuhr · C. Stührk · B. Münch · F. W. M. R. Schwarze · M. Schubert

Received: 2 March 2011 / Published online: 26 August 2011

Abstract The visualization and the quantification of microscopic decay patterns are important for the study of the impact of wood-decay fungi in general, as well as for wood-decay fungi and microorganisms with possible applications in biotechnology. In the present work, a method was developed for the automated localization and quantification of microscopic cell wall elements (CWE) of Norway spruce wood such as bordered pits, intrinsic defects, hyphae or alterations induced by white-rot fungus *Physisporinus vitreus* using high-resolution X-ray computed tomographic microscopy. In addition to classical destructive wood anatomical methods such as light or laser scanning microscopy, this method allows for the first time to compute the properties (e.g., area, orientation and size distribution) of CWE of the tracheids in a sample. This is essential for modeling the influence of microscopic CWE on macroscopic properties such as wood strength and permeability.

Introduction

Wood-decay fungi degrade their substrate, a complex anisotropic material featuring several hierarchical levels of organization from macroscopic (e.g., growth ring) over

M. J. Fuhr (✉) · C. Stührk
Institute for Building Materials, Computational Physics for Engineering Materials,
ETH Zurich, Schafmattstrasse 6, HIF E18, 8093 Zurich, Switzerland
e-mail: mfuhr@ethz.ch

M. J. Fuhr · C. Stührk · F. W. M. R. Schwarze · M. Schubert
EMPA, Swiss Federal Laboratories for Materials Science and Technology, Wood Laboratory,
Group of Wood Protection and Biotechnology, Lerchenfeldstrasse 5, 9014 St Gallen, Switzerland

B. Münch
EMPA, Swiss Federal Laboratories for Materials Science and Technology,
Group Concrete Technology, 8600 Dübendorf, Switzerland

the mesoscopic (e.g., set of wood cells) down to the microscopic and nanoscopic scale (e.g., wood cells and fibrils) by extracellular, degradative enzymes. They play an important role in natural ecosystems by recycling carbon and minerals fixed in plants. Thereby, they cause a significant damage to the wood structure and limit the possible use of wood as building material. Besides their role as biodeteriorators, wood-decay fungi can be used for biotechnological applications.

Recent investigations have shown that wood-decay fungi have many valuable biotechnological purposes in the pure and applied wood sciences (Schwarze 2008; Mai et al. 2004; Messner et al. 2002). Alterations in the cell wall structure and/or the distribution of the cell wall constituents are reflected in the plasticity of the wood degradation modes of different fungi (Schwarze 2008; Deflorio et al. 2005). The specificity of their enzymes and the mild conditions under which degradation proceeds potentially make them suitable agents for wood modification such as biopulping, bioremediation or bioincising (Majcherczyk and Hüttermann 1988; Messner et al. 2002; Schwarze 2009).

The biotechnological process of bioincising is a promising approach for improving the uptake of preservatives and wood-modification substances by refractory wood due to the degradation of bordered pits by the white-rot fungus *Physisporinus vitreus* (Pers.: Fr.) P. Karst. (Schwarze and Landmesser 2000; Schwarze et al. 2006). Furthermore because of its exceptional pattern of degradation, *P. vitreus* is successfully used to improve the acoustic properties of the tone wood of Norway spruce wood (*Picea abies* L.) used for music instruments by selectively delignifying the secondary walls without affecting the middle lamellae, even at advanced stages (Schwarze et al. 2008; Spycher et al. 2008). However, a successful up-scaling of biotechnological processes in which *P. vitreus* is used to improve substrate properties requires a set of investigations for the identification and detection of important growth parameters (Schubert et al. 2009, 2010; Schubert and Schwarze 2010) and the elucidation of the wood—fungus interactions (Lehringer et al. 2010). Hence, the visualization and quantification of microscopic decay patterns are of interest for the study of wood-decay fungi in general as well as for wood-decay fungi and microorganisms with possible applications for biotechnology. However, the quantification of microscopic cell wall alterations (e.g., their size distribution in space and time) is difficult, because of the opacity of wood and the heterogeneity of its structure.

Classical destructive methods for analyzing wood-decay fungi include light and electron microscopy of thin microtome sections. The advantages of the latter methods are the elucidation and interpretation of wood-decay patterns with the help of specific staining techniques (Schwarze 2007). However, classical microscopy techniques only provide two-dimensional (2D) information and do not allow the quantification of alterations in the cell wall structure. Yet, the growth of fungi in wood is a complex three-dimensional (3D) process due to the diverse alignment of wood cells and the distribution of nutrients. In order to successfully model the growth and impact of wood-decay fungi, more quantitative information on the distribution of fungal activity at the microscopic level in space and time is required (Fuhr et al. 2011).

At the microscopic scale, non-destructive techniques based on X-ray computed tomographic (XCT) microscopy have been mostly used in wood research for 3D investigation of mycelial expansion and the impact of wood-decay fungi. In XCT, the beam attenuation is acquired either by absorption or by scattering according to the atomic number of the constituents at each volume element (voxel). The 2D projections are subsequently reconstructed into a 3D attenuation map. McGovern (McGovern et al. 2010) measured the mass loss of wood specimens using XCT with a voxel size of approximately 0.34 mm^3. Illman and Dowd (1999) and Van den Bulcke et al. (2009) analyzed the density and structure of incubated wood applying high-resolution XCT microscopy. Van den Bulcke et al. (2008) identified single hypha of *Aureobasidium pullulans* with a diameter of approximately 10 μm in wood using high-resolution XCT microscopy. However, an automated separation of fungus and wood was not accomplished. It seems that confocal laser scanning microscopy (CLSM) is the appropriate technique to analyze the 3D structure of mycelium in wood, because of the capacity to separate fluorescence-stained fungi from the wood substrate during measurement (Stührk et al. 2010; Dickson and Kolesik 1999). However, the penetration depth of the laser light into wood is limited and the cell wall damages are not clearly visible, because of the weak autofluorescence of wood. Therefore, the use of high-resolution XCT microscopy for analyzing the impact of wood-decay fungi is suggested.

To the best of the authors' knowledge, the present work describes for the first time a computer-based automated procedure for the localization and quantification of cell wall elements (CWE) such as bordered pits, intrinsic defects and alterations induced by *P. vitreus* by means of high-resolution XCT microscopy. The quantitative information arising from this procedure allows to, e.g., analyze the distribution of the fungal activity of *P. vitreus* in the late and early wood of Norway spruce depending on the incubation conditions, which is essential for the successful manufacture of fungally modified wood.

Materials and methods

Wood and fungus

Defect-free heartwood from a Norway spruce tree (*Picea abies* [L.] Karst.) grown in Switzerland is used. The three alignments of wood cells are longitudinal (parallel to the fiber), radial (perpendicular to the fiber) and tangential (parallel to the growth rings). There are mainly two types of cells in softwoods: tracheids and rays. The cell walls of tracheids consist of several layers denoted as secondary wall S_1, S_2, S_3 and primary wall (PW) from the lumen (i.e., voids within the cells) to the middle lamella (ML) forming the border of two adjacent tracheids. In order to transport water and nutrients in longitudinal and radial direction, the cell lumina are connected via bordered and simple pits.

Specimens with dimensions of approximately 400 μm (radial) × 10 mm (tangential) × 6 mm (longitudinal) were produced with a microtome. All specimen faces, except the radial ones, were subsequently coated by brushing (Nuvovern ACR

Emaillack, Walter Mäder AG, Killwangen, Switzerland). After 24 h, the procedure was repeated to guarantee a solid sealing. Subsequently, the specimens were conditioned for 2 weeks at 22°C and 50% relative humidity (RH). Thereafter, the specimens were sterilized with hot steam (121°C, 20 min and 2 bar) and placed on a 'feeder block' of Scots pines (*Pinus sylvestris*) previously colonized with the white-rot basidiomycete *Physisporinus vitreus* Empa strain 642. Specimens were incubated under sterile conditions for 7 weeks at 22°C and 70% RH. After incubation, the specimens were cut into elongated wood prisms of approximately 400 µm (radial) × 400 mm (tangential) × 6 mm (longitudinal) using a microtome.

For the tomographic experiments, the samples were glued onto cylindrical sample holders using double-side adhesive tape, the longitudinal axis of the sample being located at the rotation axis of the tomographic stage.

Synchrotron tomographic microscopy

Synchrotron radiation facilities provide photon beams of energy densities that outrange conventional X-ray sources by orders of magnitude. Among other benefits, the high brilliance and brightness of synchrotron-based X-rays enable tomographic microscopy at sub-micrometer scale.

In the present study, tomographic experiments were performed at the TOMCAT beam line (tomographic microscopy and coherent radiology experiments) at the synchrotron radiation facility Swiss Light Source (SLS) at the Paul Scherrer Institute (PSI) in Villigen (Switzerland). The TOMCAT beam line operates in both absorption and phase-contrast mode. Phase-contrast tomography analyzes the Zernike phase contrasts of the X-ray beam induced by refraction (Neuhäusler et al. 2003) and is preferable for materials with low absorption contrast such as wood. Trtik et al. (2007) and Mannes et al. (2010) demonstrated the use of phase-contrast tomography for the analysis of 3D structures in Norway spruce wood down to the microscopic level.

In order to minimize dehydration of the specimen during measurements a climatic chamber to control the air humidity at 95% RH (Derome et al. 2010) was used. The temperature remained constant during measurements at 25°C. For each specimen, a set of 1,501 projections over 180° was acquired with a photon energy of 9.9 and 20.2 keV for absorption or phase-contrast mode, respectively. The X-rays were converted into visible light by a YAG/Ce 20-µm scintillator and projected to a charge coupled device (CCD) featuring a resolution of 2,048 × 2,048 pixels and a dynamic range of 14 bit. The nominal edge length of the cubic voxels was 0.37 µm using an optical objective with the magnification (20×) and a field of view of 0.75 × 0.75 mm. The total scanning time was approximately 15 min for both, absorption and phase-contrast mode. Stampanoni et al. (2006) provide further technical specifications for TOMCAT.

The reconstruction of the original projections into a stack of 2,048 transverse sections termed tomograms was based on filtered-back-projection using the Parzen filter supporting noise suppression. The tomograms are 16-bit gray-level TIFF images. The projection values were initially corrected with dark- and flat-field images, and the attenuation values thereof were obtained by Lambert inversion.

Stripe artifacts originating from defective detector pixels were eliminated (Munch et al. 2009) and centering artifacts remedied.

Analysis of tracheid cell wall elements

Figure 1 illustrates the cell wall analysis process, and Fig. 2 presents the core algorithm. The original data, a stack of n subsequent tomograms of the specimen, are displayed in Fig. 1a, the data processing yielding the CWE in Fig. 1b–d. Initially, the ROI of each tracheid is manually identified in the 3D tomograms. The 3D tracheid objects are subsequently mapped into 2D by applying a cylindrical projection, each point representing the mean attenuation of the cell wall voxels at an angle α, referring to the centre of gravity of the tracheid. The resulting tracheidal 2D map is a gray-level image of size $n \times s$, where $s \sim 2 \cdot \pi/\alpha$, in which regions of low attenuation values (i.e., CWE) are clearly visible. After segmentation, the distribution of the CWE size and the orientation was determined.

First, a region of interest (ROI) was selected and transformed into a binary mask separating air (black pixels) and wood material (white pixels). Segmentation was based on gray-level thresholding using Otsu's method (Otsu 1979). Figure 1b shows the original tomograms after applying a morphological closing operation using a spherical structuring element (SE) with the radius of 3 pixels, in order to remove

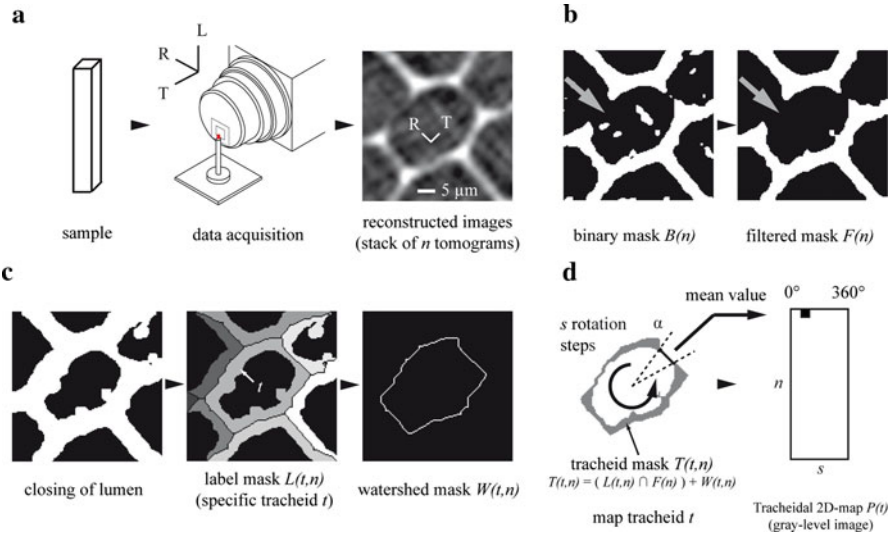

Fig. 1 Schematic workflow from (**a**) tomographic experiment to (**b–d**) quantification of cell wall elements. **a** Acquisition of original data, a stack of n subsequent tomograms and manual identification of an ROI. **b** Segmentation of the tomograms to a binary mask and removing of artifacts. **c** Closing of the cell lumina in the filtered mask in order to obtain a label mask and a watershed mask to identify the pixels corresponding to a specific tracheid. **d** Construction of the tracheid mask and mapping procedure. The 3D tracheid object is subsequently mapped into 2D using a cylindrical projection, where each point represents the mean attenuation of the cell wall voxels at an angle α, referring to the centre of gravity of the tracheid. Based on the resulting tracheidal 2D map, which is a gray-level image of size $n \times$ s, it is possible to segment and determine the distribution of the CWE size and orientation

```
program Size_Distribution
#Read Data
I <- Read Stack of n Tomograms
Ic <- Crop ROI of I

#Construction 2D Map
for i to n do
    B <- Compute binary mask of Ic(n)
    Bc <- Morphological closing of B
    F(n) <- Remove objects < p pixels from Bc
end Return Filtered mask (F)

Fc <- Morphological closing of F
for i to n do
    S <- Compute skeleton of Fc(n)
    Sr <- Remove spur pixels from S
    L(n) <- Compute label mask from Sr and Fc
end Return Label mask L

t <- Choose specific tracheid
for i to n do
    L(t,n) <- Find all pixels of tracheid t in L(n)
    W(t,n) <- Compute watershed of tacheid t
    Compute tracheid mask T(t,n) = ( L(t,n) ∩ F(n) ) + W(t,n)
    P(t,n) <- Normal cylindric projection P(t,n)
end Return Normal cylindrical projection P(t)

#Size distribution
Pb(t) <- Construct binary image of P(t)
Compute size distribution of cell wall elements in Pb(t)
end program Size_Distribution
```

Fig. 2 Core algorithm for computing the size distribution of cell wall elements of a tracheid

small objects mainly originating from noise (Gonzalez et al. 2009). The resulting filtered mask is the basis for the segmentation and mapping of the tracheids.

Tracheids were segmented by constructing the watersheds between adjacent and closed lumina (Meyer 1994). Since the lumina might not be closed because of CWE (arrow in Fig. 3a), a morphological closing operation using a SE of $3 \times 3 \times 150$ pixels was applied (Fig. 1c) prior to watershed construction. Subsequently, each spanning cluster is labeled as shown by the colors in Fig. 1c. The obtained label mask of each tomogram makes the segmentation of a tracheid in the filtered mask possible and therefore the construction of a 3D tracheid mask, which is finally used to select and map the cell wall voxels to a tracheidal 2D map using a cylindrical projection. Figure 1d illustrates this process for one of the tomograms.

Results and discussion

In order to demonstrate the potential of the method, single tracheids of an ROI with the size of $125 \times 125 \times 400$ pixels were analyzed using synchrotron XCT in

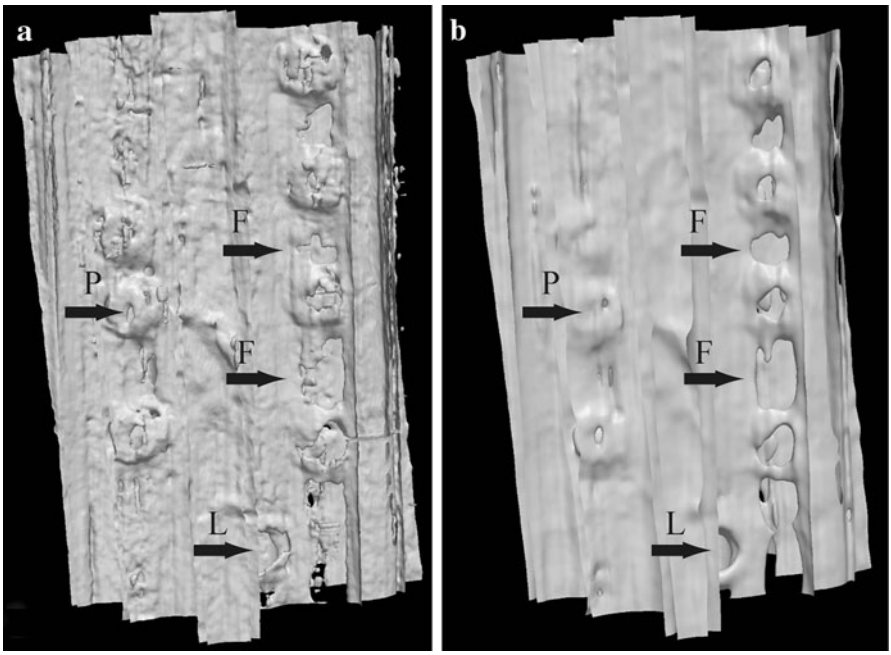

Fig. 3 ROI with a size of 125 × 125 × 400 pixels of a specimen incubated with *P. vitreus* for 8 weeks. The sample was measured using the synchrotron tomographic microscopy in (**a**) absorption and (**b**) phase-contrast mode and visualized by isosurfaces. The clusters of pixels with a very low attenuation indicate cell wall elements (CWE) such as pits (P), intrinsic defects or cell wall alterations may be induced by *P. vitreus* (F,L)

absorption (Fig. 3a) and phase-contrast mode (Fig. 3b) visualized by isosurfaces in Fig. 3a and b, respectively. CWE such as bordered pits (P), intrinsic defects or cell wall alterations induced by *P. vitreus* (F, L) were marked. The tracheidal 2D map of this tracheid is shown in Fig. 4a. The CWE are clearly visible and their segmentation was possible (Fig. 4b). Figure 4c shows the histogram of the CWE areas. Their mean attenuation can be interpreted as a measure of cell wall damage as shown in the inset. The results revealed that the tracheid's lateral surface of approximately 9,800 μm^2 had a total number of CWE of 18 with an area of approximately 285 μm^2, which relates to approximately 3% of the tracheid's lateral surface. The largest and the smallest CWE had areas of 72 and 0.05 μm^2, respectively. Most of the CWE were smaller than 40 μm^2. In addition, most CWE occurred in the tangential cell walls (Fig. 4a, b), and different shapes of CWE were recorded in tangential and radial cell walls. Larger CWE showed a lower mean attenuation than smaller CWE.

The detection and computing of the CWE revealed clusters of pixels with a very low attenuation as illustrated in the tracheidal 2D map (Figs. 3b, 4a). However, the shape of the cell wall and of the 'holes' strongly depends on the constant value for the isosurfaces (Fig. 3a, b) and the binary mask of the tracheidal 2D map (Fig. 4a). Thus, for future measurements, it is necessary to compare the tracheids before and

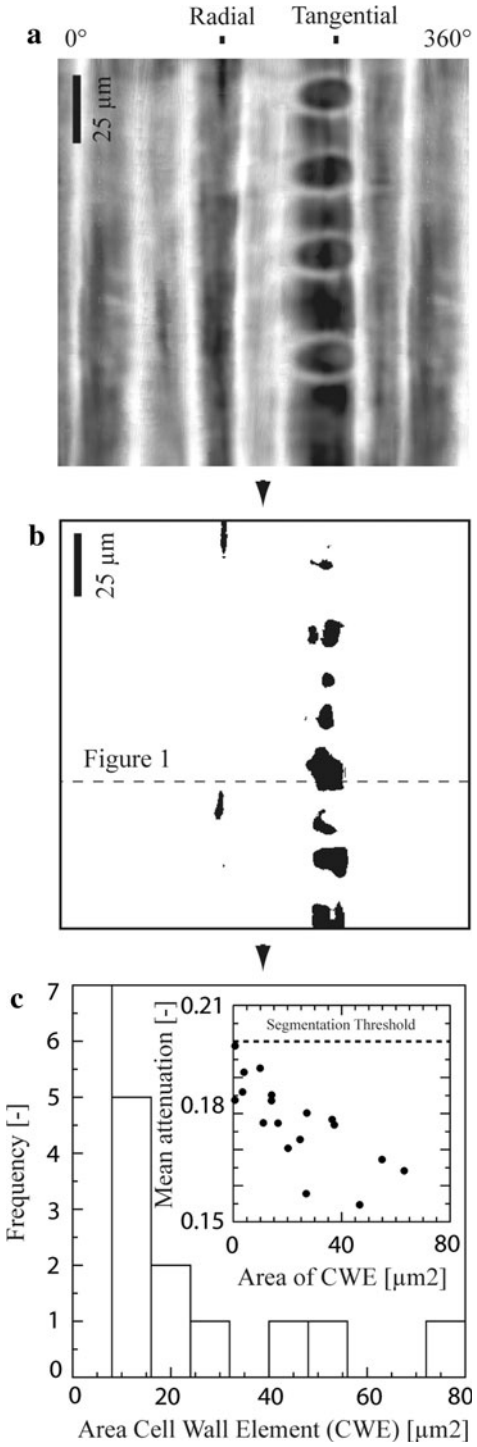

Fig. 4 Quantification of cell wall elements (CWE). **a** *Dark colors* in the tracheidal 2D map correspond to a low attenuation of the beam and therefore to a low density of the cell wall. The pits and cell wall alterations induced by the white-rot fungus *P. vitreus* are clearly visible. **b** Identification of the CWE by the construction of a threshold-based binary mask of the tracheidal 2D map. The tomogram of Fig. 1 corresponds to the *marked row* (*dashed line*). **c** An automated segmentation of CWE allows analyzing e.g., their size distribution. The *inset* shows the area of the CWE plotted against their mean attenuation

after fungal exposure in order to identify alterations of the cell wall accurately. Therefore, the scanning procedure may be time-consuming, but recent developments make laboratory-based phase-contrast XCT microscopy available (Mayo et al. 2010).

Since tracheids exhibit a complex 3D shape, the presented cylindrical projection distorts the cell wall and an elliptic cylindrical map projection might be more adequate. Furthermore, there is more noise in the absorption than in phase-contrast-based tomograms, which makes analysis more difficult. Therefore, using phase-contrast-based tomographic microscopy is suggested. Nevertheless, the analysis shows pits and cell wall alterations that might be induced by fungal activity, because the pattern of the damages was similar to those found in semi-thin light microscopy sections of incubated wood samples by Lehringer et al. (2010). It was found that most of the cell wall alterations were located in the vicinity of bordered pits and that the size distribution in Fig. 4c shows a concentration of pixels with low attenuation to large CWE's such as cell wall alterations. This result corresponds with the findings of Lehringer et al. (2010), and according to his classification system, it was possible to classify the cell wall and bordered pits (indicated by L in Fig. 3a, b) as 'strongly degraded'.

Despite the inherent structure of wood, fungi-degraded woody tissues and decay types fall into three categories according to their mode of degradation of the woody cell walls. Traditionally, wood decomposition by fungi is usually classified into three categories based on micro-morphological and chemical characteristics of decay resulting in different patterns of degradation of the cell wall: soft rot, brown rot and white rot, the latter being subdivided into simultaneous rot and selective delignification as caused by e.g., *P. vitreus* (Schwarze 2008). Finally, the presented method has the potential to identify and quantify those cell wall alterations caused by different decay types and additionally other objects within wood such as bordered pits, intrinsic defects or hyphae by comparing the wood sample before and after fungal incubation.

Conclusion

The authors presented a method to analyze and quantify microscopic CWE such as pits, intrinsic defects and cell wall alterations induced by *Physisporinus vitreus*. Their analysis focused on Norway spruce tracheids degraded by the white-rot fungus *P. vitreus*. The CWE were clearly visible, and it was possible to segment and determine the distribution of the CWE size and orientation.

It was found that most of the cell wall alterations were located in the vicinity of the bordered pits, and the computed size distribution shows a concentration of pixels with low attenuation to large CWE such as cell wall alterations. However, in addition to this classical wood anatomical method, this approach allowed for the first time to compute the properties (e.g., area, orientation and size distribution) of cell wall elements of each tracheid of a specimen, which is essential for linking the influence of microscopic cell wall elements to macroscopic system properties such as wood strength or permeability.

Therefore, in the future, the fungal activity of *P. vitreus* in Norway spruce samples will be systematically measured for different incubation periods, and the evolution of its impact on the cell wall structure will be modeled. The obtained models are essential to simulate the permeability changes of infected wood in order to optimize the choice of pellet concentration and reaction times that are required to induce a certain degree of wood permeability by *P. vitreus*. Furthermore, the presented method facilitates the development and calibration of mathematical models to optimize the impact of wood-decay fungi for biotechnological applications in pure and applied wood sciences.

Acknowledgments We acknowledge contributions and support of (in alphabetical order) Francois Gaignat, Hans Herrmann, Christian Lehringer, David Mannes, Peter Niemz, Pavel Trtik and Falk Wittel. We thank Masuru Abuku and Frederica Marone for their assistance during the measurements and Dominique Derome for supplying the climatic chamber. The authors express their gratitude to the Swiss National Foundation (SNF) No. 205321-121701 for its financial support.

References

Deflorio G, Hein S, Fink S, Spiecker H, Schwarze FWMR (2005) The application of wood decay fungi to enhance annual ring detection in three diffuse-porous hardwoods. Dendrchronologia 22:123–130

Derome D, Griffa M, Koebel M, Carmeliet J (2010) Hysteretic swelling of wood at cellular scale probed by phase-contrast X-ray tomography. J Struct Biol 173(1):180–190

Dickson S, Kolesik P (1999) Visualisation of mycorrhizal fungal structures and quantification of their surface area and volume using laser scanning confocal microscopy. Mycorrhiza 9(4):205–213

Fuhr MJ, Schubert M, Schwarze FWMR, Herrmann HJ (2011) Modeling hyphal growth of the wood decay fungus *Physisporinus vitreus*. Fungal Biol. doi:10.1016/j.funbio.2011.06.017

Gonzalez RC, Woods RE, Eddins SL (2009) Digital image processing using MATLAB. Gatesmark Publishing, Tennessee

Illman B, Dowd B (1999) High resolution microtomography for density and spatial information about wood structures. In: Bonse U (ed) Proceedings of SPIE on developments in X-ray tomography II. Society of Photo-Optical Instrumentation Engineers, Washington, DC., pp 198–204

Lehringer C, Hillebrand K, Richter K, Arnold M, Schwarze F, Militz H (2010) Anatomy of bioincised Norway spruce wood. Int Biodeterioration Biodegradation 64(5):346–355

Mai C, Kües U, Militz H (2004) Biotechnology in the wood industry. Appl Microbiol Biotechnol 63(5):477–494

Majcherczyk A, Hüttermann A (1988) Bioremediation of wood treated with preservative using white-rot fungi. In: Bruce A, Palfreyman JW (eds) Forest products biotechnology. Taylor and Francis, London, pp 129–140

Mannes D, Marone F, Lehmann E, Stampanoni M, Niemz P (2010) Application areas of synchrotron radiation tomographic microscopy for wood research. Wood Sci Technol 44(1):67–84

Mayo SC, Chen F, Evans R (2010) Micron-scale 3D imaging of wood and plant microstructure using high-resolution X-ray phase-contrast microtomography. J Struct Biol 171(2):182–188

McGovern M, Senalik A, Chen G, Beall F, Reis H (2010) Detection and assessment of wood decay using x-ray computer tomography. In: Tomizuka M (ed) San Diego, CA, USA. SPIE, p 76474B

Messner K, Fackler K, Lamaipis P, Gindl W, Srebotnik E, Watanabe T (2002) Biotechnological wood modification. In: Proceedings of the international symposium on wood-based materials, part 2. Vienna University, Vienna, pp 45–49

Meyer F (1994) Topographic distance and watershed lines. Signal Proces 38(1):113–125

Munch B, Trtik P, Marone F, Stampanoni M (2009) Stripe and ring artifact removal with combined wavelet—Fourier filtering. Optics Express 17(10):8567–8591

Neuhäusler U, Schneider G, Ludwig W, Hambach D (2003) Phase contrast X-ray microscopy at 4 keV photon energy with 60 nm resolution. J Physique IV (Proceedings) 104:567–570

Otsu N (1979) A threshold selection method from gray-level histograms. IEEE Trans Sys Man Cyber 9:62–66

Schubert M, Schwarze FMWR (2010) Evaluation of the interspecific competitive ability of the bioincising fungus *Physisporinus vitreus*. J Basic Microbiol. doi:10.1002/jobm.201000176

Schubert M, Dengler V, Mourad S, Schwarze FWMR (2009) Determination of optimal growth parameters for the bioincising fungus *Physisporinus vitreus* by means of response surface methodology. J Appl Microbiol 106(5):1734–1742

Schubert M, Mourad S, Schwarze FWMR (2010) Radial basis function neural networks for modeling growth rates of the basidiomycetes *Physisporinus vitreus* and *Neolentinus lepideus*. Appl Microbiol Biotechnol 85:703–712

Schwarze F (2007) Wood decay under the microscope. Fungal Biol Rev 1:133–170

Schwarze FWMR (2008) Diagnosis and prognosis of the development of wood decay in urban trees. ENSPEC, Melbourne

Schwarze F (2009) Enhanced uptake of wood modification agents in 'bioincised' wood. In: The international research group on wood protection

Schwarze FWMR, Landmesser H (2000) Preferential degradation of pit membranes within tracheids by the basidiomycete *Physisporinus vitreus*. Holzforschung 54(5):461–462

Schwarze FWMR, Landmesser H, Zgraggen B, Heeb M (2006) Permeability changes in heartwood of *Picea abies* and *Abies alba* induced by incubation with *Physisporinus vitreus*. Holzforschung 60(4):450–454

Schwarze FWMR, Spycher M, Fink S (2008) Superior wood for violins—wood decay fungi as a substitute for cold climate. New Phytol 179(4):1095–1104

Spycher M, Schwarze FWMR, Steiger R (2008) Assessment of resonance wood quality by comparing its physical and histological properties. Wood Sci Technol 42(4):325–342

Stampanoni M, Groso A, Isenegger A, Mikuljan G, Chen Q, Bertrand A, Henein S, Betemps R, Frommherz U, Böhler P, Meister D, Lange M, Abela R (2006) Trends in synchrotron-based tomographic imaging: the SLS experience. Proc SPIE 6318(1):63180M

Stührk C, Fuhr M, Schubert M, Schwarze F (2010) Analyzing hyphal growth of the bioincising fungus *Physisporinus vitreus* with light-, confocal laser scanning- and, synchrotron X-ray tomographic microscopy. International Group on Wood Preservation, IRG 1020438. Biarritz, France, 2010. http://www.irg-wp.org/documents.htm

Trtik P, Dual J, Keunecke D, Mannes D, Niemz P, Stähli P, Kaestner A, Groso A, Stampanoni M (2007) 3D imaging of microstructure of spruce wood. J Struct Biol 159(1):46–55

Van den Bulcke J, Masschaele B, Dierick M, Acker JV, Stevens M, Hoorebeke LV (2008) Three-dimensional imaging and analysis of infested coated wood with X-ray submicron CT. Int Biodeterioration Biodegradation 61(3):278–286

Van den Bulcke J, Boone M, Van Acker J, Van Hoorebeke L (2009) Three-dimensional X-ray imaging and analysis of fungi on and in wood. Microsc Microanal 15(5):395–402